

Highly Selective Novel Heme Oxygenase-1-Targeting Molecules Discovered by DNA-Encoded Library-Machine Learning Model beyond the DEL Chemical Space

Shuai Han^{*1}, Xinyun Guo¹, Min Wang¹, Huan Liu¹, Yidan Song¹, Yunyun He¹, Kuang-Lung Hsueh¹, Weiren Cui¹, Wenji Su¹, Letian Kuai², Jason Deng^{*2}.

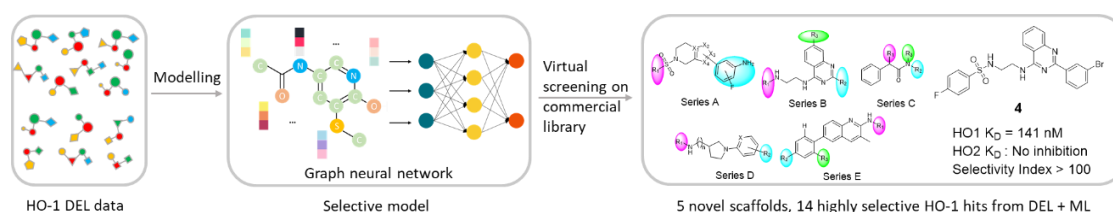
¹WuXi AppTec (Shanghai) Co., Ltd., 240 Hedan Road, Shanghai 200131, China

²WuXi AppTec, 22 Strathmore Road, Natick, MA 01760, USA

*Corresponding authors. Email: han_shuai@wuxiapptec.com; Jason.Deng@wuxiapptec.com

ABSTRACT

DNA-encoded library (DEL) technology has proven to be a powerful method for discovering novel inhibitors for diverse targets. Particularly when combined with machine learning (ML), the DEL-ML workflow expands the chemical space and enhances cost-effectiveness, offering new opportunities to find desired hit molecules. Heme oxygenase-1 (HO-1), primarily a heme-degrading enzyme, has been identified as a potential therapeutic target in diseases such as cancer and neurodegenerative disorders. Despite years of study, the HO-1 inhibitor toolbox remains limited. Here, we report the discovery of five series of novel scaffold HO-1 inhibitors using a DEL-ML workflow that emphasizes the model's uncertainty quantification and its domain of applicability. The DEL-ML model demonstrated a strong ability to extrapolate to novel chemical spaces by identifying new structures. Approximately 33% of the predicted molecules, validated by biophysical assays, had a binding affinity of $K_D < 15 \mu\text{M}$, with the strongest affinity being 141 nM. Fourteen tested molecules showed over 100-fold selectivity towards HO-1 over Heme oxygenase-2 (HO-2). These molecules are also structurally novel compared to the reported HO-1 inhibitors. Further, binding mode simulations via docking provided insights into the possible selectivity rationale of some selective series.



INTRODUCTION

Heme oxygenase (HO) degrade heme into biliverdin, Fe^{2+} and carbon monoxide; while HO-1 and HO-2 are major isozymes of the HO family. HO-1 is an inducible enzyme whose expression can be regulated by different stress stimuli, including various pro-oxidants and pro-inflammatory mediators¹. HO-2 is broadly expressed in many kinds of tissues like brain, testis and liver, which functions as maintaining the iron homeostatic, regulating redox metabolism and cellular messaging¹. Studies have shown the anti-inflammatory and antioxidant role of HO-1, which implied

HO-1 as a potential target in some chronic inflammation disease²⁻⁴. Except for its cytoprotective role in various oxidative stress environment, HO-1 is also deemed as an emerging target for cancer therapy⁵. HO-1 overexpression is often observed in prostate, renal, colon, lung, breast and glioma cancers⁶⁻¹¹. Cancer disease progression and poor prognosis are also believed to be associated with HO-1's high expression level^{5, 12}. These studies implied the potential values of selective HO-1 inhibitors in some cancer therapy. Although the search for HO-1 inhibitors started in the early 2000s¹³, only two classes of HO-1 inhibitors are reported to date: 1) Metalloporphyrin(Figure 1a), analogues of heme(Figure 1b). This type of inhibitors usually bind to other heme-containing enzymes in human thus suffering from low selectivity and potential toxicity. 2) Azole-based derivatives (Figure 1c-1d). This type of inhibitors often contains an azole substructure like imidazole, which is responsible for chelating iron in heme when binding with HO-1. However, the imidazole core is not prone to modifications¹². Azole-based derivatives also suffers from low to moderate selectivity towards HO-2^{12, 13}. So far, there has been a lack of potent HO-1 selective molecules in the research community. Therefore, finding such highly selective HO-1-target molecules will provide invaluable chemical probes for researchers to further profile HO-1's intricate biological role in human diseases.

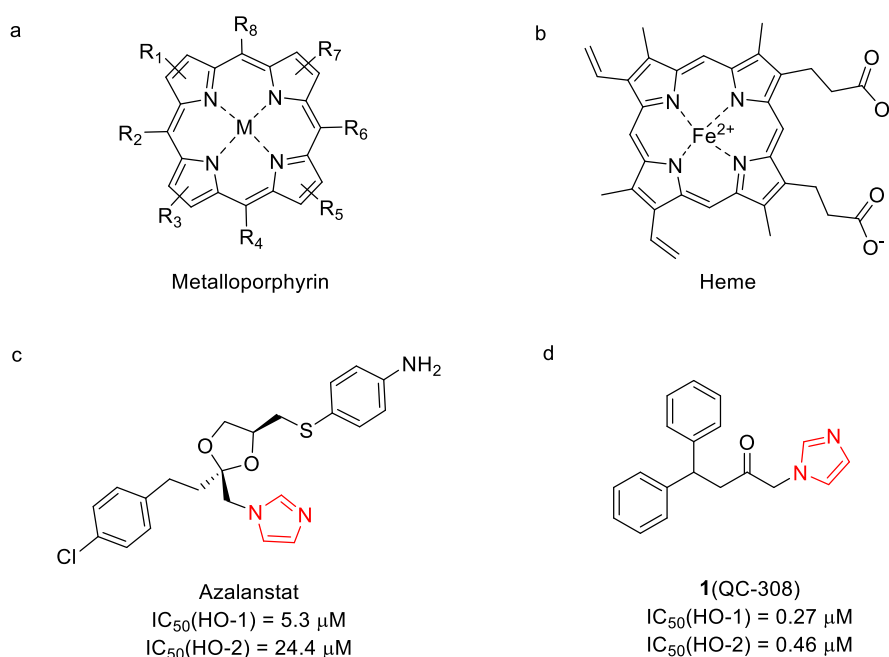


Figure 1. Structures of two major types of HO-1 inhibitors.

DEL has been evolving for several decades since its first proposal in 1992¹⁴. The progress and application cases in drug discovery have proved that DEL has become a widely used tool for hit identification, with an increasing number of clinical candidates originating from DEL screen. For instance, two DEL hits targeting RIPK1¹⁵ and sEH¹⁶ from GSK have entered Phase 2a for clinical study. In collaboration with WuXi AppTec, Westlake University identified highly potent non-covalent inhibitors of SARS-CoV-2 3CLpro through DEL screening¹⁷, which were further developed to clinical candidate WPV01. The molecule has reached phase 3 clinical trial as of this writing. Moreover, DEL technology has expanded into new application areas in recent years, including covalent drug discovery¹⁸ and PROTACS¹⁹.

From a technical perspective, DEL offers unique advantages as a fast and cost-effective approach

for screening, especially for novel targets. Compared to conventional high-throughput screening (HTS) approaches, where constructing HTS libraries can be difficult, time-consuming, and expensive, often limited to a few million compounds, DEL employs combinatorial chemistry. This allows for library sizes to reach hundreds of millions to billions of chemical diversities through 3 or 4 rounds of chemical reactions. Each DEL molecule's unique DNA tag enables efficient affinity-based screening in a single tube. Potential binders to the protein of interest are enriched and identified through next-generation sequencing and tag-to-structure decoding. However, DEL has some gaps. A notable drawback is the requirement for resynthesis of discrete DNA-free molecules identified from the DEL library, a potentially lengthy process involving new reaction planning and material procurement. Recent efforts to improve DEL molecule confirmation include using affinity selection mass spectrometry (ASMS) with high-throughput parallel resynthesis of DNA-conjugated molecules for rapid validation of potential DEL hits²⁰. Advances in technology are increasingly bridging the gap between DEL screening data and the generation of discrete molecules for wet-lab confirmation.

Using artificial intelligence, especially deep learning methods to accelerate early drug discovery have attracted much attention in drug discovery field these years. DEL data is endowed with huge quantity and high consistency within a single screening experiment, which is an ideal data generator for deep learning based modelling methods. Traditional post-selection DEL data analysis, although has proven its effectiveness in many successful cases, is still limited by the scale of molecules considered and introduced bias, which makes it difficult to fully utilize the subtle patterns in the DEL selections¹⁵. Besides, sometimes the identified DEL hits may have unfavorable physicochemical properties like large molecular weights or high logP. Kevin *et al.*²¹ have already shown the implementation of deep learning model for DEL screening data can achieve high hit rate on several targets beyond DEL chemical space. The final hits discovered by this method not only showing the novelty but also possess good physicochemical properties. Katherine *et al.*²² further demonstrated a regression approach learning DEL enrichment. Although this method cannot generalize to new chemical structures, the models can effectively denoise DEL data due to the novel uncertainty-aware loss function used during training²². Recent effort exploring usage of DEL data includes a new paradigm DEL-Dock²³, which combines target 3D structure information with DEL molecules ligand-based information. A compositional deep probabilistic model of DEL data, DEL-Compose, was also reported by this team recently²⁴. This model provides a robust tool in consideration of pharmacophores information for DEL data analysis.

Although multiple machine learning methods were reported to mine the DEL data, no research regarding to achieving high selectivity over a counter target using DEL based virtual screening was reported. Here for novel and selective hits discovery of HO-1, we performed DEL screening and further trained a deep learning model accounting for HO-1's selectivity over HO-2 using the DEL screening data and then performed virtual screening in commercial libraries. The model showed a very high classification capability between negative and positive with a precision-recall curve AUC (PRC-AUC) score of 0.95. Final validation results also imply our model can find diverse high affinity and selectivity hits for HO-1. Second round of hits expansion by testing multiple analogues of the 11 active hits further identified 8 additional active analogues. Preliminary structure activity relationship (SAR) was also discussed.

RESULTS AND DISCUSSION

DEL Screening Condition Setup To find highly selective hits of HO-1 against HO-2, HO-2 (ferric-heme bound form, Holo HO-2) was set as counter target when performing DEL screening on HO-1 (ferric-heme bound form, Holo HO-1). We mainly designed four different conditions covering main target HO-1 and counter target HO-2 (Table 1). Conditions containing HO-1 and HO-1 plus its active site inhibitor QC-308 were set for the identification of HO-1 all site binders and HO-1 allosteric binders respectively. Condition with protein HO-2 only were set as counter condition. And condition without any proteins was set as No-Target-Control (NTC) or negative condition. For further data analysis and machine learning modelling, we use conditions 1 & 2 as positive conditions and conditions 3 & 4 as negative conditions.

Table 1. DEL screening condition setup.

Condition	1	2	3	4
Target	Holo HO-1	Holo HO-1	Holo HO-2	NTC
Additives	/	20 μ M QC-308	/	/

DEL Data Curation We aimed to build a binary classification model. The DEL data thus need to be labeled into positives and negatives based on their screening results. HO-1 DEL screening data were preprocessed by a customized data curation workflow: 1) Labeling. Based on the screen performance and data distribution, the binding signal binder were identified from the non-binders as well as the noise data that had high statistical uncertainty. The signals were defined by bespoke cutoff values on copy count and enrichment factor²⁵. For each of the conditions, we further identified the positive and negative conditions based on the screening logic setup and then different cutoffs for positive and negative conditions were set. Positive and negative data were data satisfying positive and negative cutoffs, respectively. Specifically, if DEL molecules' copy and enrichment²⁵ are above the negative cutoff for negative conditions, they will be labeled as negative and the remaining data from signal data pool will be labeled as positive. 2) Data removal or addition. Generally, DEL molecules with possible DNA tag-dependent binding will be removed from our data pool. These DEL molecules were identified by mixing DNA barcode-only libraries into our whole DEL library superpool before screening were performed. 3) Downsampling and oversampling. For DEL screening data, the major part of the dataset will be negative data. The ratio of positive and negative data will be adjusted to about 1:10 by downsampling negative data, to help stabilize the model training against imbalanced data. The ratio of positive to negative data was not adjusted to 1:1 to create a balanced dataset. This approach reflects the realistic screening scenario where typically only a small fraction of the library molecules are likely to be potential positives. To decrease the false positive rate of the final prediction, negative data were fed to the model as much as possible. Despite the negative data from the aforementioned negative conditions, we also added "diluted DEL data", which was washed away during DEL screening, into negative dataset to increase the coverage of negative chemical space. Positive data were also oversampled based on their copy and enrichment performance to ensure the highly enriched DEL molecules got higher weights during model training. 4) Enumeration. Finally, all the processed DEL data will be enumerated to get their desired product SMILES. Full length DEL molecules will be used as our final training data. The final dataset size was about 5.5 million. It would be applied to a graph neural network to train a classifier model.

DEL Data Partitioning First, a holdout dataset representing 5% of the entire data were split from original labeled dataset to ensure unbiased evaluation of models. The remaining dataset were split into training, validation and test dataset by ratio of 8:1:1. All splits were done by a scaffold split method (Figure 2). Although other splitting methods²⁶ like random split, stratified split and time split, as well as cycle/synthon-based split^{22, 24} designed for DEL scenario were reported, we found the scaffold split method offers adequate solution when it comes to select models for best generalizability and potential ability to extrapolation beyond the DEL chemical space.

Deep Learning Model Training A binary classifier model was trained after data curation. Graph neural network was selected for the modelling. ReLU²⁷ was chosen as activation function and dropout regularization was also applied during training to reduce possible overfitting. Model ensemble technique was applied with multiple model instances and training data samples. Three independent model initializations were used. Each model trained over 50 epochs and the one epoch checkpoint with the highest validation PRC-AUC score was selected. Train loss was also monitored to see if the models converged. At last, all three models reached a high average PRC-AUC score of ~0.95 on validation, test and holdout dataset (Figure 2).

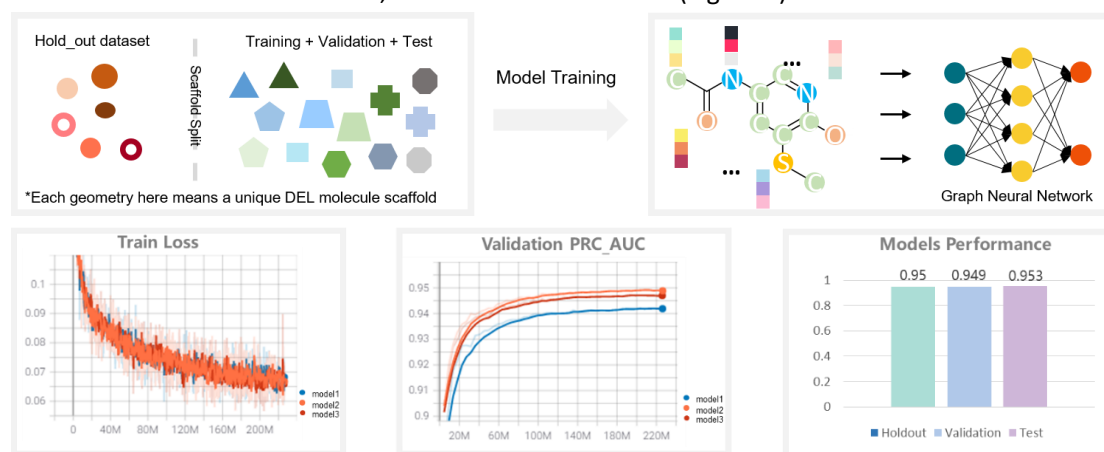


Figure 2. Model training and performance.

Virtual Screening Virtual screening were then performed on commercial libraries including WuXi Galaxi and Mcule. Model ensemble was used and the final predicted positive hits were further analyzed by our proprietary compounds picking workflow including uncertainty qualification (UQ) filter, physicochemical property filter, domain of applicability (DA) filter and in-house liability substructure filter. Then diversity selection by using clustering was also applied to ensure the structure diversity of selected compounds. Final compounds list was reviewed by medicinal chemist to ensure the removal of possible unstable or promiscuous hits. After that, we also visualized the chemical space distribution of the final list compared with the HO-1 positive training dataset by using Uniform Manifold Approximation and Projection (UMAP) method²⁸. Result showed that final 392 picked compounds have a very diverse structure distribution (Figure 3a). Some picked compounds overlapping with the training compounds (dots in red circle) on UMAP indicate that they are similar with training data in chemical space. While we also discovered some other compounds (dots in blue circle) which are dissimilar with training data in chemical space. This visualization result demonstrated that our workflow can find potential hits beyond DEL chemical space. We further calculated the cosine distance distribution between picked compounds and training dataset. Compounds were represented by feeding the structures into the trained model and the last layer of the graph neural network were output as the compound

representations (latent space). The similarity between compounds were measured by cosine similarity of two vectors. For all the picked compounds, we found their nearest neighbor in positive training dataset by calculating their similarities, which is defined as nearest neighbor similarity. Then the nearest neighbor distances (1- nearest neighbor similarity) of the 392 picked compounds with training dataset were shown by density plot (Figure 3b). Two peaks in the density plot also showed consistent results as UMAP: similar and dissimilar compounds, compared with training data, were found at the same time in the final compounds list.

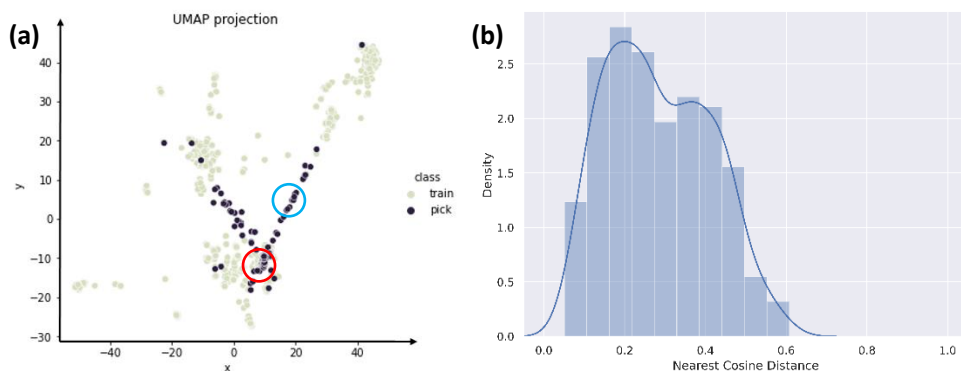


Figure 3. Chemical space analysis of picked compounds. (a) UMAP analysis of picked compounds' chemical space. Compounds were represented as Morgan fingerprint (ECFP6) and undergo dimension reduction and visualized by UMAP. (b) Nearest neighbor cosine distance distribution of picked compounds with training set. Compounds were represented as latent space and cosine distance was calculated as 1-cosine similarity.

Biophysics Validation Out of the top 50 potential binders from machine learning suggestions, we purchased 32 compounds for subsequent Surface Plasmon Resonance (SPR) binding analysis. These compound prediction scores are shown in Table S1. HO-1/2 protein was synthesized as avi-tagged constructs and immobilized on streptavidin sensor chip for SPR. Among the tested compounds, binding of 8 compounds to HO-1 or HO-2 were confirmed with SPR, with K_D ranging from 141 nM to 11 μ M (Table 2). Fitting curves of these active hits are presented in Figure S1.

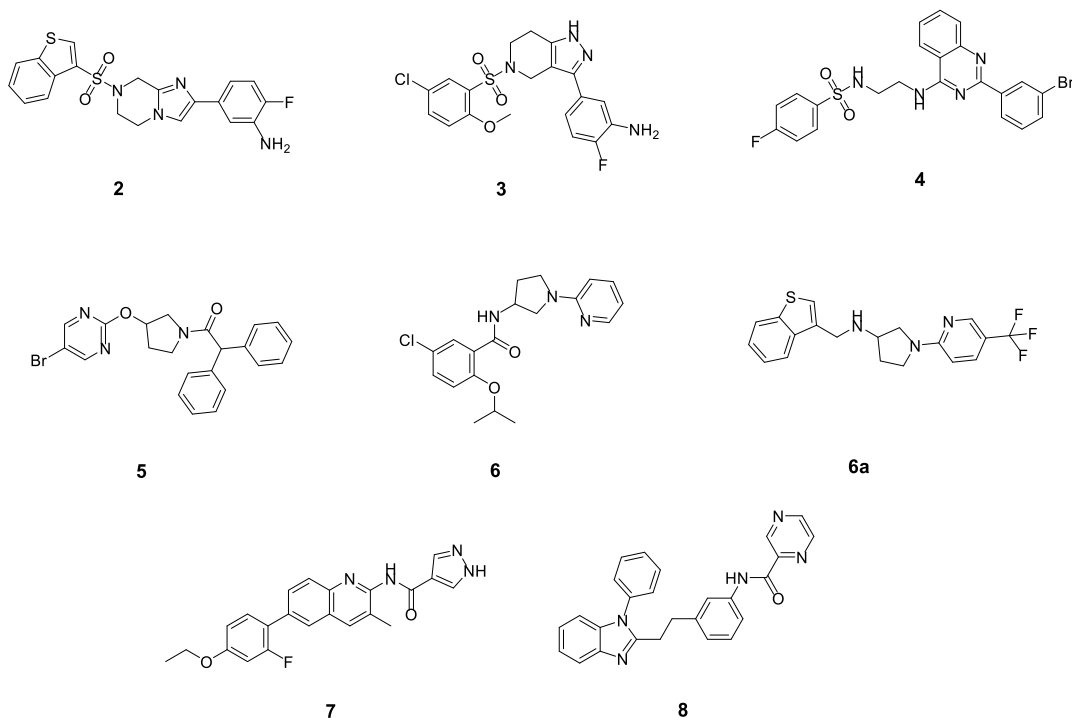


Figure 4. 8 validated hits structures from DEL based virtual screening.

Table 2. SPR data of 8 validated hits from virtual screening.

Target		HO-1		HO-2	
Compound ID	Fit model	K _D (nM)	Fit model	K _D (nM)	
2	Steady state	648	Steady state	N.D.	
3	Steady state	5100	Steady state	N.D.	
4	Steady state	141	Steady state	N.D.	
5	Steady state	1420	Steady state	N.D.	
6	Steady state	11000	Steady state	N.D.	
6a	Steady state	7590	Steady state	N.D.	
7	Steady state	9290	Steady state	N.D.	
8	Steady state	794	Steady state	119	

N.D.: Binding not detected.

Second round hits validation Based on the discovery of first 8 active hits, we further conducted similarity search among compounds with UQ calibrated score (UQCS) greater than 0.5. UQCS is a prediction score calibrated with UQ metric. Here we calculated the average score of 3 prediction scores from 3 models and their standard deviation. UQCS equals average score minus three times of standard deviation. Fingerprint (ECFP6) was used as structure representation. Tanimoto similarity between these compounds and 8 active hits were calculated. Compounds were ranked by Tanimoto similarity and top 10% were selected (Tanimoto similarity ranging from 0.4 to 0.76) and finally reviewed by chemist to find out close analogues of the 8 active hits. Finally only 11 compounds were available from vendors and we validated these compounds' K_D with HO-1 and HO-2 by SPR (Figure S2). Among them, 8 compounds (Figure 5) were found out binding activities to HO-1 and other 3 completely lost their binding activities (Table 3). Combined all validation results together, we got the preliminary SAR information for some series.

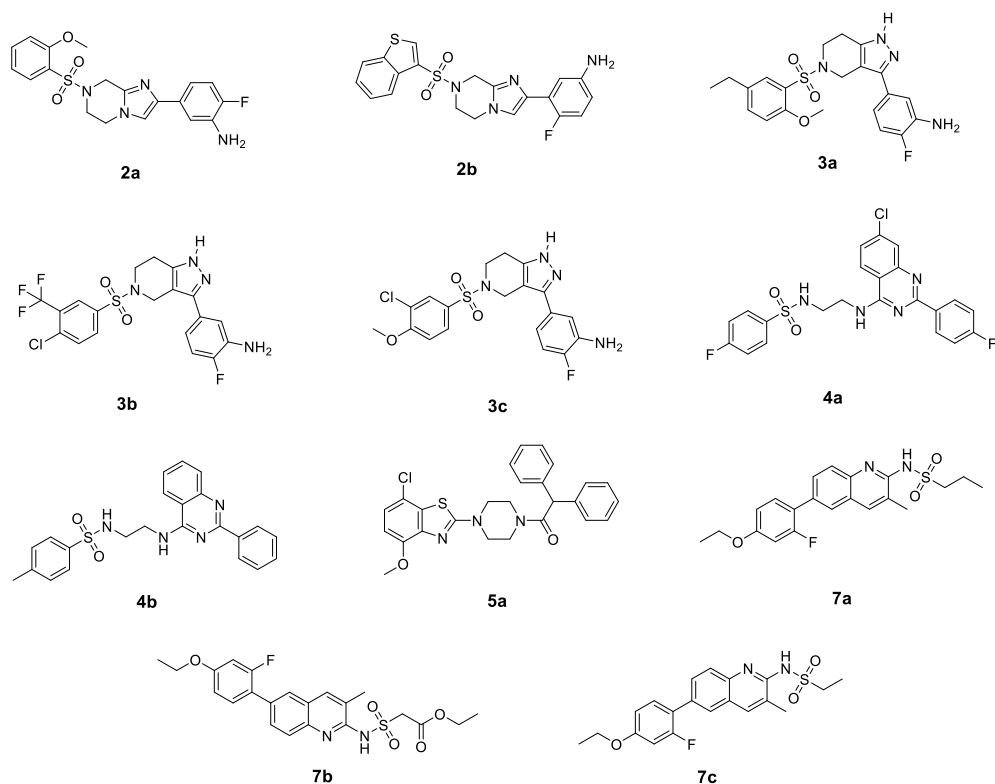


Figure 5. 11 compounds structures in second round hits validation.

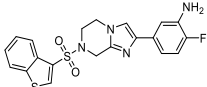
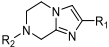
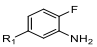
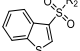
Table 3. SPR data of second round hits.

Target	HO-1		HO-2	
Compound ID	Fit model	K _D (nM)	Fit model	K _D (nM)
2a	Steady state	N.D.	Steady state	N.D.
2b	Steady state	N.D.	Steady state	N.D.
3a	Steady state	7930	Steady state	N.D.
3b	Steady state	1840	Steady state	N.D.
3c	Steady state	703	Steady state	N.D.
4a	Steady state	692	Steady state	N.D.
4b	Steady state	6920	Steady state	N.D.
5a	Steady state	17100	Steady state	20800
7a	Steady state	3790	Steady state	N.D.
7b	Steady state	19800	Steady state	N.D.
7c	Steady state	N.D.	Steady state	N.D.

N.D.: Binding not detected.

Preliminary SAR analysis Among the 43 purchased compounds, we collected all 16 active compounds and 7 of their analogues to analyze the preliminary SAR (Table 4). There are at least 8 different scaffolds discovered, which can be further classified into 5 series (Figure 6, series A-E). Most of the scaffolds have at least 2 analogues. Although detailed SAR information needs to be obtained by testing more analogues of different scaffolds, we obtained a preliminary SAR understanding of some scaffolds because of their close similarity to each other. Tetrahydroimidazo[1,2-a]pyrazine scaffold (**2**, **2a-2b**) and tetrahydro-1H-pyrazolo[4,3-c]pyridine scaffold (**3**, **3a-3c**) have a high Tanimoto similarity of 0.84 (using MACCS key fingerprint). These 2 scaffolds share similar R₁ substituent and fluorine & amino substituted benzene. So we represented their structures by a Markush structure series A (Figure 6). Similar methods were applied among other compounds showed in Table 4 and finally 4 other Markush structures series B-E were drawn (Figure 6). For series A, in general X₄ substitution (**3**, **3a-3c**) is better than X₃ substitution (**2**, **2a-2b**). X₄ substitution also shows high selectivity towards HO-1. Series A with X₄ substitution can tolerate various 3,6- or 3,4- substituted benzene as R₁; Series A with X₄ substitution seems to be sensitive to both the R₁ and position of fluorine substitution on the benzene. When R₁ is benzothiophene, minor change of fluorine substitution from *para* to *ortho* position completely abolished its binding with HO-1 and HO-2. For the quinoline derivatives (series B, **4**, **4a-4b**), R₁ and R₂ can be various halogenated benzene. R₃ is tolerable to chlorine substitution. **4** is the most potent HO-1 binder among all the 16 active compounds. This series also shows high selectivity towards HO-1. Most of compounds from series C (**5**, **5a-5b**) have a common diphenyl subgroup, which is an important pharmacophore of QC-308. Since QC-308 was added to the training data and given high weights, it's not surprising that compounds similar to it were discovered. It's worth noting that **5** achieves high selectivity on HO-1 while it's not the case for **5a**. This series compounds are likely to bind to HO-1 in a similar pattern¹² with QC-308 due to the structure similarity. Two phenyls locate in the "Western Region" and aromatic heterocyclic ring points to heme ("Eastern Region")¹². This kind of binding may indicate a new optimization direction, modifying the "Eastern Region" but not the "Western Region" binding part, for highly selective HO-1 binder development. Pyrrolidine based derivatives (series D, **6**, **6a-6c**) can also serve as a selective scaffold towards HO-1 when the aromatic ring connecting to pyrrolidine is pyridine derivative. For quinoline scaffold (series E, **7**, **7a-7d**), R₁ is critical for its activity. It seems that when R₁ is sulfone or carbonyl derivatives, the backbone length should be greater than 3 (**7**, **7a-7b**). The R₁ backbone length of **7c** and **7d** is 3, resulting in completely activities lost. Quinoline scaffold is also a selective HO-1 scaffold which shows no binding with HO-2 in all derivatives. Compound **8** has potent activity on HO-1 and even shows better potency on HO-2. Because of the unique scaffold it can't be included in any 5 series mentioned above. Among all these 16 active HO-1 binders, 14 of them is highly selective towards HO-1.

Table 4. Activity summary of 23 tested compounds from model prediction.

ID	Structure	HO-1 K _D (nM)	HO-2 K _D (nM)	Scaffold	R ₁	R ₂	R ₃	Selectivity Index (SI)
2		648	N.D.				-	> 100

2a		N.D.	N.D.				-	-
2b		N.D.	N.D.				-	-
3		5100	N.D.				-	>100
3a		7930	N.D.				-	>100
3b		1840	N.D.				-	>100
3c		703	N.D.				-	>100
4		141	N.D.				H-R3	>100
4a		692	N.D.				Cl-R3	>100
4b		6920	N.D.				H-R3	>100
5		1420	N.D.					>100
5a		17100	20800					1.2
5b		N.D.	N.D.					

6		11000	N.D.			H-R ₂	-	>100	
6a		7590	N.D.				-	>100	
6b		N.D.	N.D.				-	-	
6c		N.D.	N.D.				-	-	
7		9290	N.D.					R ₃ -F	>100
7a		3790	N.D.					R ₃ -F	>100
7b		19800	N.D.					R ₃ -F	>100
7c		N.D.	N.D.					R ₃ -F	-
7d		N.D.	N.D.					R ₃ -	-
8		794	119	-	-	-	-	-	0.15

N.D.: Binding not detected.

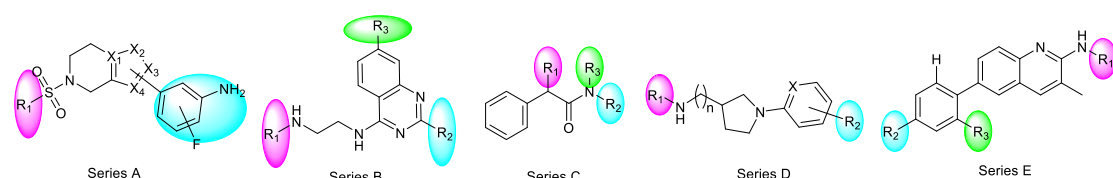


Figure 6. 5 series summarized from 23 compounds structures

Analysis of hits discovered by DEL based virtual screening In order to evaluate the structural novelty of newly discovered hits from virtual screening, we compared the similarity between 16 active HO-1 hits ($K_D < 20 \mu\text{M}$) and 2 representative HO-1 inhibitors (Azalanstat and QC-308). Both full compounds and Bemis-Murcko scaffolds were used to calculate their similarities. Tanimoto similarity matrix using ECFP6 representation were generated as shown in Figure 7a-7b. All hits coming from virtual screening have a very low similarity (< 0.3) compared with Azalanstat and QC-308 both in terms of full compounds (Figure 7a) and Bemis-Murcko scaffolds (Figure 7b). This result indicated that these newly discovered HO-1 hits are novel scaffold compounds.

We further explored the relationship between tested compounds' similarities to the nearest neighbor in positive training dataset and cumulative hit rate in Figure 8a-8b. Different similarity cutoffs ranging from 0 to 1 with step 0.1 were set and corresponding cumulative hit rate were calculated for compounds with the nearest neighbor similarity lower than the cutoff. Hit rate can

be also defined under different binding affinity cutoffs. When we used ECFP6 as the compound representation, we measured their similarities by Tanimoto similarity with the result shown in Figure 8a. When the Tanimoto similarity cutoff is 0.4, we can still observe a meaningful hit rate under different binding affinity cutoffs. It indicated that potential hits can still be enriched even they are dissimilar with the positive training dataset. This result further demonstrated the generalization capability of our workflow.

Similarly, when compounds were represented by the latent space and similarities were calculated by cosine similarities, we got the result in Figure 8b. Except for the similar curve trend, the turning point moved from 0.3 to 0.6. Our results demonstrated that the hit rate of validated machine learning (ML) compounds positively correlated with latent space-based similarity above a 0.6 unit cosine similarity. Conversely, this correlation was not observed with the ECFP6-based similarity. This suggests that the mechanism underlying ML model predictions differs from that of traditional ECFP-based similarity searches, a finding consistent with recent reports indicating underwhelming hit rates using ECFP²⁰. Additionally, our findings suggest that latent space-based similarity may serve as a guide to improve overall hit rates.

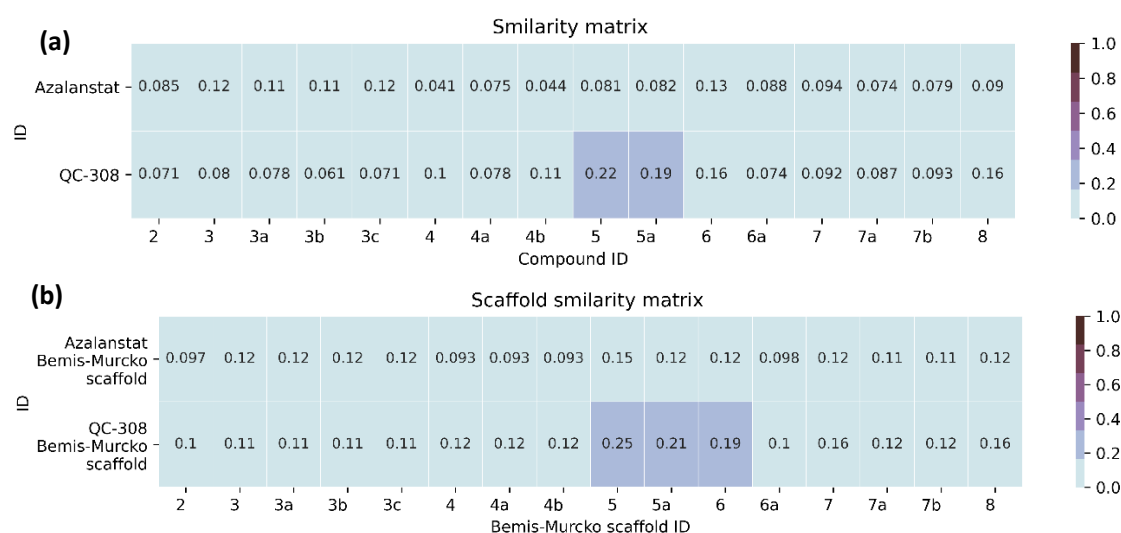


Figure 7. Structure novelty of 16 actives compared with 2 known HO-1 inhibitors. Similarity matrix between 16 active hits' (a) full structures, (b) Bemis-Murcko scaffolds and 2 known HO-1 inhibitors.

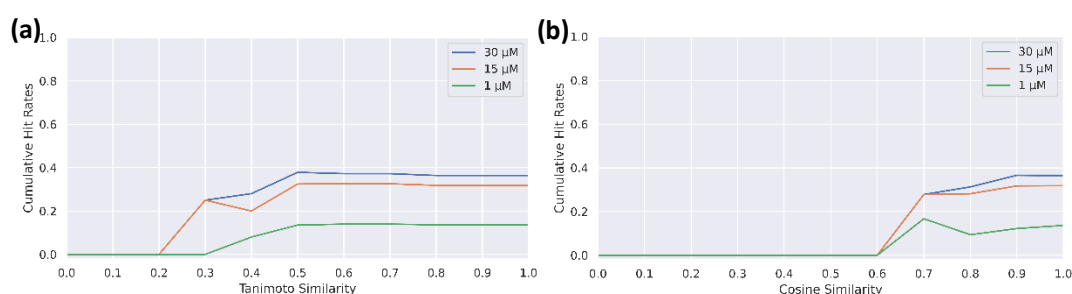


Figure 8. Cumulative hit rates under different activity cutoffs with x-axis of (a) Tanimoto similarity of predicted active compounds (ECFP6) to the training DEL dataset (b) Cosine similarity of predicted active compounds (latent space) to the training DEL dataset.

Comparison between selective and nonselective model performance In order to better understand the selectivity profile of the model, we conducted retrospective study by comparing

the performance between selective and nonselective models using 43 tested compounds. The nonselective model was trained by labeling DEL data enriched in conditions 1, 2 and 3 as positive data and that in condition 4 as negative data (Table 1). Then 3 nonselective models were trained by 50 epochs. Other hyper-parameter settings (like learning rate, batch size and number of layers *etc.*) were the same with previous selective models. Training loss and model performance after training were shown in Figure 9. Nonselective models showed an even higher average PRC-AUC scores of ~ 0.997 on holdout, validation and test dataset compared with selective models (Figure 2). 43 compounds were predicted by 3 nonselective models and 10 of them is predicted as positive (Table S2). Finally, only 2 compounds (**6**, **6a**) were validated as selective binders. The success rate is 20%, while for selective models 32.6% compounds (14 out of 43) were validated as selective binders. 2 selective compounds predicted by nonselective models belong to series D. This result indicated that although nonselective models perform very well in holdout dataset PRC-AUC score, they still miss many important selective structure patterns like series A, B, C and E discovered by selective models. By simply setting counter targets condition (in this case, HO-2) as negative and applying a similarity based analogue finding approach, we finally identified 14 highly selective HO-1 binders among all 16 active HO-1 binders ($K_D < 20 \mu\text{M}$). This result may, at least in this case, prove the effectiveness of selectivity strategy in our workflow.

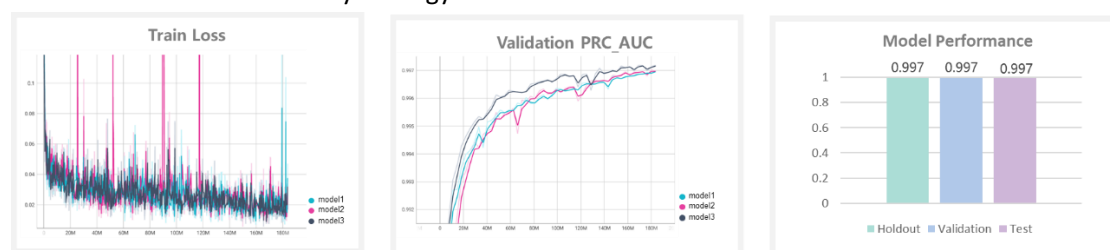


Figure 9. Nonselective models training loss and performance.

Binding mode simulation via docking In order to better understand the molecular interaction and selectivity profile of some series compounds, we performed molecular docking using MOE2022 to explore their possible binding modes. We chose the most potent hit compound **4** to study its possible binding mode. Series B represents a highly selective scaffold towards HO-1 and compound **4**'s binding mode may provide some insights for the selectivity profile of this series compounds. Compound **4** binds to HO-1 in a different binding mode compared with 3HOK's original ligand QC-80 (Figure 10a). There is no metal chelating interaction of compound **4** and HO-1. Fluorine substituted benzene of compound **4** inserts into the "Western Region" formed by residues Phe166, Leu54, Phe167, Val50 and Phe47, which is the main binding pocket of QC-80. A hydrogen bond is also observed between the sulfamide of compound **4** and Arg136. Besides, quinazoline of compound **4** stretches to the "Northeastern Region" formed by residues Ala28, Ala31, Glu32, Ile211 and Glu215, and occupies a similar pocket compared with QC-80. Bromine substituted benzene of compound **4** partially occupies "Western Region" of HO-1, which may be a unique binding mode of HO-1 inhibitors to date. Since the hydrophobic property of "Western Region", hydrophobic substituents like fluorine (**4a**) and methyl (**4b**) can still retain activity. Removal of hydrophobic fluorine and chlorine substituents from **4a** resulted in a remarkable decrease in activity (**4b**). By comparing the binding pocket of HO-1 and HO-2, we found that HO-2's pocket volume (551 \AA^3 , calculated by PyVol²⁹) is smaller than HO-1's (911 \AA^3 , calculated by PyVol²⁹). The heavy atom distances between compound **4** and some key pocket residues like Arg156, Phe234,

Phe53 and Phe57 are smaller than 3.5 Å (Figure 10b), which means clashes formed. It may explain the high selectivity profile of this scaffold towards HO-1. Taking advantages of the differences of “Northeastern Region” in HO-1 and HO-2 may be a feasible way to design more selective HO-1 inhibitors.

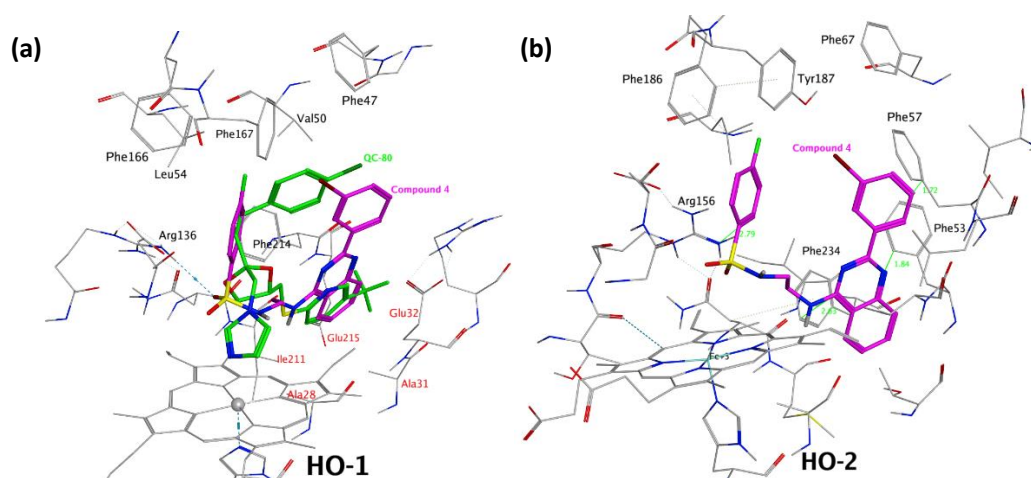


Figure 10. Binding poses simulation of **4** with HO-1&HO-2 via docking. (a) Docking pose of **4** in HO-1 and pose alignment with QC-80. Protein residues are represented as gray sticks. QC-80 and **4** are represented as green and magenta, respectively. The “Western Region” and “Northeastern Region” of HO-1 are shown by black and red labeled residues, respectively. Hydrogen bond is shown as cyan dotted line. (b) Docking pose of **4** in HO-2. The green lines show the distances between **4** and some nearby residues.

CONCLUSIONS

In summary, this study demonstrates the effectiveness of utilizing extensive DEL screening data in conjunction with deep learning models for the discovery of novel, drug-like hits beyond the conventional DEL chemical space. Our approach, which incorporates selectivity information during the modeling process, has proven to be a successful strategy for identifying highly selective hits. The analysis of cumulative hit rates under different representation methods revealed that latent space representations of molecular structures are superior to traditional fingerprint representations. This suggests a more nuanced approach to detecting underlying chemical structure patterns, moving beyond the traditional chemist's intuition in structure similarity comparison. Our method also demonstrated the ability to identify novel active scaffolds outside the original DEL chemical space. Although the current selectivity approach during modeling is qualitative, incorporating selectivity information by assigning counter target data as negative has been effective. Future work may explore more quantitative methods during deep learning modeling, such as using ratios between target condition enrichment and counter target condition enrichment. The discovery of five novel and selective series of HO-1 inhibitors marks a significant step forward in the search for selective and potent HO-1 inhibitors.

METHODS

DEL Library Construction DNA encoded libraries used in this study are started with a short double-stranded DNA oligonucleotide, and carried out through split-and-pool cycles that consist

of a DNA barcode ligation step and a chemical synthesis step. The short double-stranded oligonucleotide, often referred to as headpiece, contains a chemical linker moiety for connecting to the small molecule moiety, and a sticky for ligation of duplex DNA barcode sequence. In general, the starting oligonucleotide is split as many reactions vessels as building blocks later applied. The codons are ligated to the headpiece by T4 ligase, after successful ligation, ethanol crash will be done to precipitate the DNA pellets. Then the pellets will be re-dissolved in reaction buffer, chemical building blocks may then be added to the vessels to append to the linker. The above cycle of encoding and synthesis is closed by pooling all the vessels into a single vessel, and the pooled product was crashed by ethanol. And then the mixture is ready for the next cycle. In general, two-cycle, three-cycle DELs are designed and synthesized as above procedure. It can enable highly efficient to collect building blocks to cover broad chemical space onto desired targets.

DEL Screening A pull-down-based approach was employed for affinity selection. The selection conditions, including both HO-1, HO-1 with an inhibitor, and HO-2 were summarized in Table 1. The procedure can be briefly summarized as: protein immobilization, DEL incubation and elution. 5 μ g biotinylated avi-tagged HO-1 or HO-2 were incubated with 20 μ L Pierce™ Streptavidin Magnetic Beads in 100 μ L immobilization buffer [1xPBS, pH 7.4] with rotation for 30 minutes. The flowthrough was discarded and the beads were sequentially subject to 1 round of wash using the immobilization buffer, 2 rounds of wash using streptavidin blocking buffer [1xPBS, pH 7.4, 20 mM biotin], and 1 additional round of wash using immobilization buffer. Next, 1 nmol WuXi proprietary DNA encoded library was incubated with the immobilized protein in selection buffer [1xPBS, pH 7.4, 1XPBS, 0.05% Tween 20, 0.1 mg/mL sheared salmon sperm DNA] for 1 hour with rotation. Flowthrough was discarded, while the beads were washed 3 times with the selection buffer. In order to elute the hit DEL molecules, the beads were resuspended in 50 μ L elution buffer [1xPBS, pH 7.4, 1XPBS, 0.05% Tween 20] and heated at 95 °C for 10 minutes. The elution was used as the input for the next round of affinity selection. The final round of elution was subjected to a standard DNA purification step and the final DEL molecules were eluted by double distilled water. The final eluted DEL sample will be amplified by standard PCR. The PCR products were purified and sequenced by the next-generation sequencing.

Similarity/distance calculation and nearest neighbor Similarity between compounds was measured either by Tanimoto similarity, Equation (1) or cosine similarity, Equation (2).

$$T(A, B) = |A \cap B| / (|A| + |B| - |A \cap B|) \quad (1)$$

Where A and B are two fingerprints with n binary attributes.

$$C(A, B) = (A \cdot B) / (|A| \cdot |B|) = \sum_{i=1}^n A_i B_i / \sqrt{\sum_{i=1}^n A_i^2} \cdot \sqrt{\sum_{i=1}^n B_i^2} \quad (2)$$

Where **A** and **B** are two non-zero vectors, A_i and B_i are the *ith* components of vectors **A** and **B**, respectively. Distance is equal to one minus similarity. We used RDKit³⁰ (v.2020.09.5) to convert compounds into Morgan fingerprints with radius set as 3 (ECFP6) and then Tanimoto similarity was calculated. For cosine similarity, compounds were fed into trained model and the last layer (1000-bit) of graph neural network were output as the compound representations. Subsequently, cosine similarity was calculated between two non-binary vectors. Nearest neighbor of a compound means the most similar compound (with highest Tanimoto/cosine similarity) to this compound in a specified compound set.

Surface Plasmon Resonance A Biacore 8K instrument was employed to conduct affinity analysis. Biacore Series S Sensor chip SA (SA: streptavidin) (GE healthcare) were employed to immobilize Avi

tagged HO-1 and HO-2. The binding of off-DNA compounds was tested in the presence of HEME. Depending on compound off-rate, some compounds were tested using multi cycle kinetic measurements with 12 different concentrations at a 2-fold dilution, including 0 concentration baseline. The rest compounds with slower off rates were tested using single cycle kinetic measurements with 9 different concentrations at a 2-fold dilution. The flow rate and association time for both multi cycle and single cycle measurements was 30 μ L per minute and 60 seconds respectively, and dissociation time was 500 and 1200 seconds for multi cycle and single cycle measurements. Biacore Insight Evaluation Software (V3.0.12) was used to analyze binding events.

Molecular Docking Published cocrystal structures of HO-1 (PDB code: 3HOK) and HO-2 (PDB code: 2QPP) were chosen as docking templates. Amber10:EHT was selected as the force field. Hydrogens were added to the proteins, and then they were subjected to further energy minimization by using QuickPrep in MOE2022³¹. During docking, ligands were flexible while receptors remained rigid. Before compounds docking, re-docking of the original ligand of HO-1 was performed. The reproducibility of the original ligand pose (RMSD<2 Å) ensured the reliability of docking program parameters setting. Compound **4** was docked into the protein by proxy triangle methods and 100 poses were scored by London dG and finally refined and scored by GBVI/WSA dG scoring function. Among the top 10 poses, final best pose was selected by combining the docking score, visual inspection and preliminary SAR information.

REFERENCE

1. Campbell, N. K.; Fitzgerald, H. K.; Dunne, A., Regulation of inflammation by the antioxidant haem oxygenase 1. *Nat Rev Immunol* **2021**, *21* (7), 411-425.
2. Chen, S.; Wang, X.; Nisar, M. F.; Lin, M.; Zhong, J. L., Heme Oxygenases: Cellular Multifunctional and Protective Molecules against UV-Induced Oxidative Stress. *Oxid Med Cell Longev* **2019**, *2019*, 5416728.
3. Lee, T. S.; Chau, L. Y., Heme oxygenase-1 mediates the anti-inflammatory effect of interleukin-10 in mice. *Nat Med* **2002**, *8* (3), 240-6.
4. Poss, K. D.; Tonegawa, S., Reduced stress defense in heme oxygenase 1-deficient cells. *Proc Natl Acad Sci U S A* **1997**, *94* (20), 10925-30.
5. Chau, L. Y., Heme oxygenase-1: emerging target of cancer therapy. *J Biomed Sci* **2015**, *22*, 22.
6. Maines, M. D.; Abrahamsson, P. A., Expression of heme oxygenase-1 (HSP32) in human prostate: normal, hyperplastic, and tumor tissue distribution. *Urology* **1996**, *47* (5), 727-33.
7. Goodman, A. I.; Choudhury, M.; da Silva, J. L.; Schwartzman, M. L.; Abraham, N. G., Overexpression of the heme oxygenase gene in renal cell carcinoma. *Proc Soc Exp Biol Med* **1997**, *214* (1), 54-61.
8. Yin, H.; Fang, J.; Liao, L.; Maeda, H.; Su, Q., Upregulation of heme oxygenase-1 in colorectal cancer patients with increased circulation carbon monoxide levels, potentially affects chemotherapeutic sensitivity. *BMC Cancer* **2014**, *14*, 436.
9. Degese, M. S.; Mendizabal, J. E.; Gandini, N. A.; Gutkind, J. S.; Molinolo, A.; Hewitt, S. M.; Curino, A. C.; Coso, O. A.; Facchinetti, M. M., Expression of heme oxygenase-1 in non-small cell lung cancer (NSCLC) and its correlation with clinical data. *Lung Cancer* **2012**, *77* (1), 168-75.
10. Noh, S. J.; Bae, J. S.; Jamiyandorj, U.; Park, H. S.; Kwon, K. S.; Jung, S. H.; Youn, H. J.; Lee, H.; Park, B. H.; Chung, M. J.; Moon, W. S.; Kang, M. J.; Jang, K. Y., Expression of nerve growth factor and heme oxygenase-1 predict poor survival of breast carcinoma patients. *BMC Cancer* **2013**, *13*,

516.

11. Gandini, N. A.; Fermento, M. E.; Salomon, D. G.; Obiol, D. J.; Andres, N. C.; Zenklusen, J. C.; Arevalo, J.; Blasco, J.; Lopez Romero, A.; Facchinetti, M. M.; Curino, A. C., Heme oxygenase-1 expression in human gliomas and its correlation with poor prognosis in patients with astrocytoma. *Tumour Biol* **2014**, *35* (3), 2803-15.
12. Fallica, A. N.; Sorrenti, V.; D'Amico, A. G.; Salerno, L.; Romeo, G.; Intagliata, S.; Consoli, V.; Floresta, G.; Rescifina, A.; D'Agata, V.; Vanella, L.; Pittala, V., Discovery of Novel Acetamide-Based Heme Oxygenase-1 Inhibitors with Potent In Vitro Antiproliferative Activity. *J Med Chem* **2021**, *64* (18), 13373-13393.
13. Vlahakis, J. Z.; Kinobe, R. T.; Bowers, R. J.; Brien, J. F.; Nakatsu, K.; Szarek, W. A., Synthesis and evaluation of azalanstat analogues as heme oxygenase inhibitors. *Bioorg Med Chem Lett* **2005**, *15* (5), 1457-61.
14. Brenner, S.; Lerner, R. A., Encoded combinatorial chemistry. *Proc Natl Acad Sci U S A* **1992**, *89* (12), 5381-3.
15. Harris, P. A.; Berger, S. B.; Jeong, J. U.; Nagilla, R.; Bandyopadhyay, D.; Campobasso, N.; Capriotti, C. A.; Cox, J. A.; Dare, L.; Dong, X.; Eidam, P. M.; Finger, J. N.; Hoffman, S. J.; Kang, J.; Kasparcova, V.; King, B. W.; Lehr, R.; Lan, Y.; Leister, L. K.; Lich, J. D.; MacDonald, T. T.; Miller, N. A.; Ouellette, M. T.; Pao, C. S.; Rahman, A.; Reilly, M. A.; Rendina, A. R.; Rivera, E. J.; Schaeffer, M. C.; Sehon, C. A.; Singhaus, R. R.; Sun, H. H.; Swift, B. A.; Totoritis, R. D.; Vossenkamper, A.; Ward, P.; Wisnoski, D. D.; Zhang, D.; Marquis, R. W.; Gough, P. J.; Bertin, J., Discovery of a First-in-Class Receptor Interacting Protein 1 (RIP1) Kinase Specific Clinical Candidate (GSK2982772) for the Treatment of Inflammatory Diseases. *J Med Chem* **2017**, *60* (4), 1247-1261.
16. Belyanskaya, S. L.; Ding, Y.; Callahan, J. F.; Lazaar, A. L.; Israel, D. I., Discovering Drugs with DNA-Encoded Library Technology: From Concept to Clinic with an Inhibitor of Soluble Epoxide Hydrolase. *ChemBiochem* **2017**, *18* (9), 837-842.
17. Hou, N.; Shuai, L.; Zhang, L.; Xie, X.; Tang, K.; Zhu, Y.; Yu, Y.; Zhang, W.; Tan, Q.; Zhong, G., Development of highly potent noncovalent inhibitors of SARS-CoV-2 3CLpro. *ACS central science* **2023**, *9* (2), 217-227.
18. Li, L.; Su, M.; Lu, W.; Song, H.; Liu, J.; Wen, X.; Suo, Y.; Qi, J.; Luo, X.; Zhou, Y. B.; Liao, X. H.; Li, J.; Lu, X., Triazine-Based Covalent DNA-Encoded Libraries for Discovery of Covalent Inhibitors of Target Proteins. *ACS Med Chem Lett* **2022**, *13* (10), 1574-1581.
19. Chen, Q.; Liu, C.; Wang, W.; Meng, X.; Cheng, X.; Li, X.; Cai, L.; Luo, L.; He, X.; Qu, H.; Luo, J.; Wei, H.; Gao, S.; Liu, G.; Wan, J.; Israel, D. I.; Li, J.; Dou, D., Optimization of PROTAC Ternary Complex Using DNA Encoded Library Approach. *ACS Chem Biol* **2023**, *18* (1), 25-33.
20. Su, W.; Ge, R.; Ding, D.; Chen, W.; Wang, W.; Yan, H.; Wang, W.; Yuan, Y.; Liu, H.; Zhang, M.; Zhang, J.; Shu, Q.; Satz, A. L.; Kuai, L., Triaging of DNA-Encoded Library Selection Results by High-Throughput Resynthesis of DNA-Conjugate and Affinity Selection Mass Spectrometry. *Bioconjug Chem* **2021**, *32* (5), 1001-1007.
21. McCloskey, K.; Sigel, E. A.; Kearnes, S.; Xue, L.; Tian, X.; Moccia, D.; Gikunju, D.; Bazzaz, S.; Chan, B.; Clark, M. A.; Cuozzo, J. W.; Guie, M. A.; Guilinger, J. P.; Huguet, C.; Hupp, C. D.; Keefe, A. D.; Mulhern, C. J.; Zhang, Y.; Riley, P., Machine Learning on DNA-Encoded Libraries: A New Paradigm for Hit Finding. *J Med Chem* **2020**, *63* (16), 8857-8866.
22. Lim, K. S.; Reidenbach, A. G.; Hua, B. K.; Mason, J. W.; Gerry, C. J.; Clemons, P. A.; Coley, C. W., Machine Learning on DNA-Encoded Library Count Data Using an Uncertainty-Aware Probabilistic

- Loss Function. *J Chem Inf Model* **2022**, *62* (10), 2316-2331.
23. Shmilovich, K.; Chen, B.; Karaletsos, T.; Sultan, M. M., DEL-Dock: Molecular Docking-Enabled Modeling of DNA-Encoded Libraries. *J Chem Inf Model* **2023**, *63* (9), 2719-2727.
24. Chen, B.; Sultan, M. M.; Karaletsos, T., Compositional Deep Probabilistic Models of DNA Encoded Libraries. *arXiv preprint arXiv:2310.13769* **2023**.
25. Kuai, L.; O'Keeffe, T.; Arico-Muendel, C., Randomness in DNA Encoded Library Selection Data Can Be Modeled for More Reliable Enrichment Calculation. *SLAS Discov* **2018**, *23* (5), 405-416.
26. Wu, Z.; Ramsundar, B.; Feinberg, E. N.; Gomes, J.; Geniesse, C.; Pappu, A. S.; Leswing, K.; Pande, V., MoleculeNet: a benchmark for molecular machine learning. *Chem Sci* **2018**, *9* (2), 513-530.
27. Agarap, A. F., Deep learning using rectified linear units (relu). *arXiv preprint arXiv:1803.08375* **2018**.
28. McInnes, L.; Healy, J.; Saul, N.; Großberger, L., UMAP: Uniform Manifold Approximation and Projection. *Journal of Open Source Software* **2018**, *3* (29).
29. Smith, R. H. B.; Dar, A. C.; Schlessinger, A., PyVOL: a PyMOL plugin for visualization, comparison, and volume calculation of drug-binding sites. *bioRxiv* **2019**, 816702.
30. *RDKit: Open-source cheminformatics.*, 2020-09-5.
31. *Molecular Operating Environment (MOE)*, 2022.02 Chemical Computing Group ULC, 1010 Sherbooke St. West, Suite #910, Montreal, QC, Canada, H3A 2R7, 2023.